Mechanism of Pb Adsorption to Fatty Acid Langmuir Monolayers Studied by X-ray Absorption Fine Structure Spectroscopy

Maxim I. Boyanov,[*,†,‡] **Jan Kmetko,**[§,||] **Tomohiro Shibata,**[†] **Alokmay Datta,**[§,⊥] **Pulak Dutta,**[§] **and Bruce A. Bunker**[†]

Department of Physics, University of Notre Dame, Notre Dame, Indiana 46556, and Department of Physics and Astronomy, Northwestern University, Evanston, Illinois 60208

The local atomic environment of lead (Pb) adsorbed to a $CH_3(CH_2)_{19}COOH$ Langmuir monolayer was investigated in situ using grazing-incidence X-ray absorption fine structure (GI-XAFS) spectroscopy at the Pb L_{III} edge. Measurements were performed at pH 6.5 of the 10^{-5} M $PbCl_2$ solution subphase, a condition under which grazing incidence diffraction (GID) revealed a large-area commensurate superstructure underneath the close-packed organic monolayer. The XAFS results indicate covalent binding of the Pb cations to the carboxyl headgroups, and the observed Pb−Pb coordination suggests that the metal is adsorbed as a hydrolysis polymer, rather than as individual Pb^{2+} ions. The data are consistent with a bidentate chelating mechanism and a one Pb atom to one carboxyl headgroup binding stoichiometry. We discuss how this adsorption model can explain the peculiarities observed with Pb in previous metal−Langmuir monolayer studies. A systematic study of lead perchlorate and lead acetate aqueous solutions is presented and used in the analysis. XAFS multiple scattering effects from alignment of the Pb−C−C atoms in the lead acetate solutions are reported.

1. Introduction

Langmuir monolayers of carboxylic acids spread on aqueous solutions have been the object of intense investigation in the past decades.[1] Interest is driven by the desire for fundamental understanding of the interactions, as well as by the technological promise of transferred ("Langmuir−Blodgett" or LB) films.[2] Langmuir systems are also studied as templates for oriented growth of crystals and as a model for the nucleation phase of biomineralization.[3,4] Previous work shows that monolayers formed over dilute metal solutions have properties quite different from those formed over pure water. The "compressed" phase is attained even at large areas per molecule, and the viscoelastic response, surface potential, refractive index, and layer transferability to solid substrates are affected appreciably by the subphase metal.[5−10] Infrared spectroscopy results suggest that the carboxyl headgroups become deprotonated and complexed as pH increases.[11,12] More recently, synchrotron grazing incidence diffraction (GID) experiments determined precise in-plane lattice parameters, chain tilt, and the layer thickness of the acid monolayer, for various aqueous metals, concentrations, and pH.[13−18] The existence of thin commensurate superstructures for some of the metals is also revealed. Attempts to correlate the lattice parameters with the cationic radii or Pauling electronegativity have not been successful.[18] Anomalous diffraction and X-ray reflectivity data suggest that Pb and Cd adsorb as hydrolysis products rather than as individual cations.[15,17] Among the metals studied in the above works, Pb can be singled out as

having the greatest influence on the monolayer by compressing it the most,[5] producing the greatest surface potential and refractive index change,[5,6,8] the largest surface loss tangent,[8] and the largest area superlattice.[17] These effects are observed at the lowest subphase pH and metal concentration for Pb.

The existing literature suggests that models in which individual cations interact with the amphiphiles may be inadequate in explaining the superstructures and the monolayer properties mentioned above. Questions remain as to what the structure of the adsorbed complex is, the nature of the adsorbent−headgroup interactions (ionic, covalent, or mixed), and the adsorbent: headgroup stoichiometry. These are all essential parameters in thermodynamic[19,20] and electrochemical[21,22] theories that model the experimental data. Most studies conclude subphase metal adsorption on the basis of circumstantial data, and there are few direct in situ confirmations that the divalent ion (and not, for instance, precipitates or the pH-controlling agent) is condensed at the interface and influencing the monolayer ordering.[23,24] Aqueous Pb, in particular, seems to have a very specific effect when compared to other divalent metals.

We report here the results from grazing incidence XAFS (X-ray absorption fine structure) experiments on a monolayer of heneicosanoic acid ($CH_3(CH_2)_{19}COOH$) spread over an aqueous $PbCl_2$ solution. This study extends previous GID work on the same system.[17] New structural and chemical information about the adsorbed Pb atoms is presented. On the basis of the XAFS data, an adsorption model of a hydrolysis trimer in which each Pb atom is bound to one carboxyl headgroup is proposed. The role of this model in explaining the results of previous Langmuir monolayer studies with Pb is discussed.

2. Experimental Procedures

2.1. Experimental Setup. XAFS experiments were carried out at the Materials Research Collaborative Access Team

* Corresponding author. E-mail: mboyanov@nd.edu.
† University of Notre Dame.
‡ Present Address: Argonne National Laboratory, Argonne, IL 60439.
§ Northwestern University.
|| Present address: Department of Physics, Cornell University, Ithaca, NY 14853.
⊥ Present address: Saha Institute of Nuclear Physics, Calcutta 700064, India.

XAFS of Pb Adsorbed to Langmuir Monolayers

J. Phys. Chem. B, Vol. 107, No. 36, 2003 **9781**

(MRCAT) beamline of the Advanced Photon Source. The beamline is equipped with a tunable undulator and a cryogenic double-crystal Si (111) monochromator.[25] A rhodium-coated mirror was used for harmonic rejection. The incident X-ray beam was defined to a vertical thickness of 0.1 mm and a 20 mm horizontal width. The Langmuir samples were studied in a total external reflection configuration, with the incidence angle set at 0.065°, slightly below the calculated critical angle of an air−water interface (0.09° at 13.6 keV photon energy). The calculated penetration depth of the evanescent wave is about 90 Å. The effect of the Pb atoms in the Stern and diffuse layers underneath the 30 Å acid monolayer on the optical properties is assumed negligible. The Pb L_{III} edge XAFS data were collected in fluorescence mode, using a sealed Stern−Heald type detector[26] filled with Kr and placed on the side of the aqueous surface (perpendicular to the beam). The continuous-scanning mode of the monochromator was used which reduces the radiation exposure during a single scan (ca. 3 min/EXAFS scan, 1 min/XANES scan). Before the XAFS experiments, GID data were collected from the Pb−Langmuir monolayer system to verify that the monolayer structure is the same as the one observed in previous GID experiments.[17] The stability of the film to radiation damage was determined by observing the changes in the GID pattern with irradiation time. The diffraction pattern was unchanged for 40 min at the intensity used, after which gradual deterioration of the superlattice peaks began. Fresh samples were thus prepared every 35 min of measurements, after careful cleaning of the trough with hexane and water, and following an identical preparation procedure. The scans were aligned by the simultaneously collected Pb foil data; the first inflection point of the absorption edge was set at 13035 eV. The derivative of the individual reference channel scans were repeatable within less than 1 eV in the XANES area. The maximum scatter between the individual scans of the monolayer sample was 2−3 eV due to the lower signal-to-noise ratio. Because the Pb−Langmuir data are produced by averaging about 35 scans, a conservative energy resolution estimate for the final data set is 1 eV. Data from consecutive scans of each sample were averaged, and the resulting data from all identical Pb−Langmuir samples were normalized and averaged. The edge energies for the samples were chosen at the inflection point, and background was subtracted using the AUTOBK program.[27]

2.2. Sample Preparation. The Langmuir monolayer preparation is outlined in a previous paper.[17] Briefly, heneicosanoic acid dissolved in chloroform was spread by gently dropping it with a syringe over the solution subphase. After evaporation of the chloroform, the monolayer was compressed with a Teflon barrier until a slight increase in the surface pressure was observed. The Langmuir trough that was used is described in detail elsewhere;[28] it is an enclosed system with Kapton windows for the incident, scattered, and fluorescence X-rays, with gas lines to maintain slight overpressure of He gas and a liquid circulator to maintain the sample temperature at 9 °C. The pH of the 10^{-5} M $PbCl_2$ subphase solution was raised to 6.5 by adding NaOH solution in 5 μL aliquots to the 300 mL solution. A single stock solution for the subphase was used throughout the study.

Powder and aqueous Pb standards were used for comparison and theory calibration in the analysis. The PbO_2 powder standard was prepared from commercially available chemicals (Sigma-Aldrich), after grinding and sieving (−400 mesh). The phase purity was checked by powder X-ray diffraction before mounting on Kapton tape. The spectrum was measured at ∼10 K. We were unable to obtain commercial red (tetragonal) PbO in

the pure crystallographic phase, so we have used an XAFS spectrum of that material from the XAFS Spectra Library at SSRL.[29] The aqueous standards were prepared with distilled deionized water (resistivity 18 MΩ cm) and analytical grade chemicals (Sigma-Aldrich) without further purification. To avoid the formation of carbonate aqua complexes and precipitates, the water was boiled to remove dissolved CO_2. All further preparation, pH adjustment, and sample mounting was carried out in an Ar-purged glovebox. The solution sample holders were sealed Plexiglas slides with Kapton film windows for transmission measurements. The samples and identification names (in quotation marks) are as follows: as a standard for hydrated Pb cation ("Pb(aq)"), a 0.2 M solution of $Pb(ClO_4)_2$ at pH 2.5 (unadjusted) was used; as a standard for Pb hydrolysis complex ("$[Pb_4(OH)_4]^{4+}$"), a 0.2 M solution of $Pb(ClO_4)_2$ at pH 6.1 (adjusted with NaOH) was prepared; as standards for aqueous Pb bound to a carboxyl group in solution, several solutions of $Pb(CH_3COO)_2 \cdot 3H_2O$ with different amounts of $NH_4(CH_3COO)$ added were prepared. The $NH_4(CH_3COO)$ was added to overload the solution with carboxyl anions, thus gradually shifting the equilibrium between hydrated lead and lead bound to carboxyl groups toward the bound species. Because XAFS measures the average local environment of all Pb atoms, it is necessary that the standards contain predominantly one species to obtain a representative spectrum for that environment. The Pb:carboxyl groups ratios and Pb concentrations are as follows: "PbAc-1", 1:2 (no additional acetate added), 0.2 M; "PbAc-2", 1:10, 0.1 M; "PbAc-3", 1:10, 0.2 M; "PbAc-4", 1:∼100, 0.1 M. Speciation of Pb in the solution standards was calculated using published hydrolysis and stability constants.[30,31]

3. XAFS Theory and Data Reduction

Extended X-ray absorption fine structure (EXAFS) spectroscopy uses the small periodic variations in the absorption coefficient above the absorption edge energy of an element to extract information about the local environment of that atom. There are complete references on the subject.[32,33] Only a short description of this theory is given here.

The EXAFS of a powder-like sample with Gaussian disorder can be derived as follows:[33]

$$\chi(k) = \sum_i \frac{(N_i S_0^2) F_i(k)}{k R_i^2} \exp\left(-2k^2\sigma_i^2 - \frac{2R_i}{\lambda(k)}\right) \times$$
$$\sin(2R_i k + \delta_i(k)) \quad (1)$$

The sum is taken over all distinguishable single and multiple scattering paths that the ejected photoelectron wave traverses in the material before it returns to the absorber atom. Here k is the electron wave vector, $k \propto \sqrt{\hbar\omega - E_0}$, E_0 is the edge energy and $\hbar\omega$ is the incident photon energy, N_i is the multiplicity of the path (coordination number in the case of single scattering), S_0^2 is the constant passive electron reduction factor, R_i is the half path length (interatomic distance in the case of single scattering), σ_i^2 is the relative mean square displacement of the path length (EXAFS Debye−Waller factor, which differs from the X-ray diffraction Debye−Waller factor), $F_i(k)$ and $\delta_i(k)$ are the effective scattering amplitude and phase shift of the scattered electron, respectively, and $\lambda(k)$ is the mean free path of the photoelectron. An energy origin shift variable ΔE_0 is added when fitting, $k \rightarrow \sqrt{k^2 - (2m\Delta E_0/\hbar^2)}$, to account for differences in the calculated and measured edge energies. As can be seen, $\chi(k)$ is a superposition of sinusoidal waves in k-space with

frequency related to the length of the scattering path. Data are usually weighed by k^n ($n = 1-3$) to emphasize different parts of the spectrum. A Fourier transform (FT) of $k^n\chi(k)$ results in peaks at close to the half path length distance that appear similar to a radial distribution function, but peak positions are shifted to smaller R values due to $\delta_i(k)$. In cases of destructive interference between neighboring shells, a peak may not be observed even though an atom is present. The contribution from multiple scattering paths can be neglected in most room temperature measurements because of thermal motion, except when the scattering atoms are aligned in a straight line (focusing multiple scattering). In the real or imaginary part of the FT the contributions corresponding to the different scattering atoms combine linearly to produce the observed features, so comparison to spectra of standards in which the features are assigned can reveal the presence of a certain atom in the unknown sample. The final structural parameters are obtained from fits of the real and imaginary parts of $FT[k^n\chi(k)]$, using model scattering amplitudes and phase shifts.

In current EXAFS analysis, $F_i(k)$ and $\delta_i(k)$ are calculated ab initio for a cluster of atoms and then calibrated by using appropriate standards with known structure. The calibrated $F_i(k)$ and $\delta_i(k)$ are then used in a fitting procedure where the structural parameters N_i, R_i, and σ_i^2 are varied until a best fit to the experimental data is achieved. The ATOMS,[34] FEFF8,[35] and FEFFIT[36] programs were used in this work. Simultaneous multiple k-weighting (k^1, k^2, and k^3) R-space fits of each spectrum were performed, which reduces the possibility of obtaining erroneous parameters due to correlations at any single k-weighting. The fit quality is characterized by two parameters: the XAFS reliability factor R, which measures the sum-of-squares difference between data and fit normalized to the experimental data, and the reduced factor χ_ν^2, which also takes into account the number of variables and noise in the data. R values of a few percent or less and a fit that visually follows the main features of the data are generally considered acceptable in XAFS analysis.[37] The χ_ν^2 should theoretically be close to 1 for a good fit.[38] In practice, it is always close to several tens or hundreds in XAFS fitting, even for a visually good fit of data from a known system. A detailed discussion on the origin of this and how it is handled to determine accurately the fitting parameter uncertainties is given in the FEFFIT documentation. Even though larger than 1, χ_ν^2 can be used for comparison between different fitting scenarios—if the χ_ν^2 reduction observed by adding a new shell or new fitting parameters is statistically significant, then the extra flexibility introduced in the fit is considered justified by the data.

When the incoming photon has energy slightly larger than the binding energy, the absorption probability is determined by the absorbing atom's density of states near the Fermi energy. Thus, the near-edge (XANES) region of the spectrum is sensitive to the valence state, bond type, bond orientation, and symmetry. Rigorous treatment to extract that information from XANES spectra is not currently possible, but comparisons with the spectra of model compounds can reveal details about the atom's bond geometry.

4. Experimental Results

4.1. Powder and Solution XAFS Standards. Fit results from the PbO and PbO$_2$ standards are listed in Table 1. These standards have relatively simple local structures for Pb^{2+} and Pb^{4+} charge states, respectively, and were used to test the ability of FEFF8 to model a known system. The EXAFS was calculated from the known crystal structures[39,40] using single scattering

Pb—O and Pb—Pb paths, where the distances of the shells were not varied independently, but a single linear lattice expansion parameter was applied to all. The fit (not shown) reproduced the spectral features in the entire fit range (1.0−4.2 Å) for both samples. The S_0^2 factors obtained for Pb^{2+} (PbO) and Pb^{4+} (PbO$_2$) at room temperature were 0.71(5) and 0.81(6), respectively. The S_0^2 was set to 0.71 in the analysis of all Pb^{2+} samples with an oxygen first shell environment.

Data from the solution standards are presented on Figure 1. A notable observation in the acetate spectra is that they all cross at the same points (isosbestic points) when overlaid together with the hydrated Pb standard. This indicates that there are only two distinct Pb species (hydrated and bound to acetate), and that only the ratio of one to the other is changing with acetate overloading. The sample most overloaded with acetate anions, PbAc-4, is thus considered to be representative of most Pb ions bound to acetate and is used to obtain structural information for the Pb−acetate aqua complex. Fit results are shown in Figure 2 and Table 1. The immediate Pb environment is fit well by an O and C shell from the bound acetate group. The obtained 4 O atoms in the first shell and 2 C atoms in the second are consistent with a bidentate-chelating binding mechanism (Figure 2a), observed also in crystal Pb acetate[41] and inferred by infrared spectroscopy in solution.[42] An interesting feature in the magnitude of the FT is the peak at 3.8 Å. It has a large amplitude, which is unlikely for EXAFS from a loosely coordinated second hydration shell in a solution complex. Another possibility is a Pb atom from Pb−Pb interactions. Testing models with an O or Pb shell at this distance does not result in satisfactory fits. The best fit is obtained using focusing multiple scattering (MS) paths from the two C atoms in the acetate group. This is additional evidence for the bidentate mechanism, as the Pb−C1−C2 straight line can only be formed when the Pb atom is bound in the acetate plane with both O atoms. In our final fit, a single distance change and σ^2 variables are used for all MS and C2 paths, and their numbers are constrained to be the same as the number of the carboxyl C1 atoms. The distance between the closer C1 and farther C2 atoms calculated from the fitted Pb−C distances is consistent with the structure of the acetate group in crystalline Pb acetate.[41] The σ^2 values for all Pb−C and Pb−O paths are about the same. The similar disorder is an indication that these atoms behave as a rigid group. All of the above supports a binding mechanism in which the Pb ion is bound by both carboxyl O atoms.

The hydrated sample, Pb(aq), shows a broad asymmetric peak in the FT, which is shifted to higher distance relative to the acetate spectra (Figure 2). The main peak is fit with an O shell from hydration water at ca. 2.6 Å (Table 1). The addition of a second, closer O shell at 2.15 Å, improves the fit at the left shoulder of the main peak. This Pb−O distance is the same as in PbO$_2$ and is at the lower end of the range of Pb−O distances found in Pb(II) oxides, hydroxides, and oxisalts.[43] The origin of this atom in the solution is unclear—a small amount of Pb may have been complexed due to impurities in the dissolved chemicals or as hydroxide. The presence or absence of this atom in the fit model does not, however, alter appreciably the fit values for the hydration shell at 2.6 Å (Table 1).

The data from the [Pb$_4$(OH)$_4$]$^{4+}$ hydrolyzed solution standard are modeled on the basis of the crystal structure of Pb$_4$(OH)$_4$-(NO$_3$)$_4$.[44] A drawing of the [Pb$_4$(OH)$_4$]$^{4+}$ complex is shown in Figure 2b. It can be described as two interleaved Pb$_4$ and (OH)$_4$ tetrahedrons, forming a distorted cubical cage. This structure is preserved in aqueous solutions.[45] Fitting of the split FT peak between $R = 3$ and 4 Å was indeed most consistent with Pb−

TABLE 1: Numerical Fit Results[a]

powders	path	CN	R (Å)	σ^2 (Å²)	ΔE_0 (eV)	χ_v^2	R, %
PbO-tetr	Pb−O	4.0	2.30(1)	0.007(1)	0.0(6)	247	1.4
	Pb−Pb	4.0	3.67(1)	0.006(1)	−2.7(7)		
	Pb−Pb	4.0	3.80(1)	0.013(5)	−2.7(7)		
	Pb−Pb	4.0	3.94(1)	0.012(4)	−2.7(7)		
PbO$_2$ (10 K)	Pb−O	2.0	2.15(0)	0.002(1)	4.4(6)	1457	2.0
	Pb−O	4.0	2.17(0)	0.001(1)	4.4(6)		
	Pb−Pb	2.0	3.38(0)	0.003(1)	3(1)		
	Pb−Pb	8.0	3.89(0)	0.003(1)	3(1)		

solutions	path	CN	R (Å)	σ^2 (Å²)	ΔE_0 (eV)	χ_v^2	R, %
PbAc-4	Pb−O	3.7(2)	2.36(1)	0.011(1)	1.8(5)	139	0.8
	Pb−C1	2.0(2)	2.92(1)	0.009(3)	7.2(5)		
	Pb−C2[b]	N_{C1}	4.47(2)	0.009(3)	7.2(5)		
	−C1−C2−[b]	$2 \times N_{C1}$	4.47(2)	0.009(3)	7.2(5)		
	−C1−C2−C1−[b]	N_{C1}	4.47(2)	0.009(3)	7.2(5)		
Pb$_4$(OH)$_4^{4+}$	Pb−O1	1.3(5)	2.37(1)	0.015(4)	4(3)	92	0.1
	Pb−O2	8(2)	2.72(1)	0.034(2)	2.3(4)		
			third→[c]	0.009(1)			
	Pb−Pb	3.0(2)	3.77(1)	0.016(1)	−5.1(4)		
Pb^{2+}(aq)[d]	Pb−O2	11.3(4)	2.59(2)	0.030(1)	−0.4(5)	302	0.5
			third→[c]	0.002(1)			
Pb^{2+}(aq)[d]	Pb−O1	0.5(2)	2.14(1)	0.003(2)	0.0(2)	73	0.1
	Pb−O2	12.7(5)	2.64(1)	0.029(1)	0.0(2)		
			third→[c]	0.006(0)			

sample	path	CN	R (Å)	σ^2 (Å²)	ΔE_0 (eV)	χ_v^2	R, %
Pb−Langm	C(COO)[e]	0.9(2)	2.91(2)	0.0096	−1.9(9)	17	1.7
	O (hydration)	14(9)	2.70	0.08(3)	−1.9(9)		
			third→[c]	0.002(3)			
	Pb (Pb + OH)[e]	2.8(9)	3.77(4)	0.016	−1.9(9)		

[a] Column headers and sample identification names are explained in the theory and experimental sections. CN = coordination number, ΔE_0 is an energy origin shift variable (see the FEFFIT documentation). Error bars are given in parentheses and show standard deviation from the value in the last digit shown (e.g., 0.71(5) = 0.71 ± 0.05). When no error bars are given, the parameter is held fixed to the listed value. The coordination numbers of the powder standards are fixed to those determined in the X-ray diffraction studies. [b] Single and multiple scattering (MS) paths associated with the farther C2 atom in the acetate group. CNs are constrained to be equal to the C1 coordination number. [c] Third cumulant, included in the fit because of the large disorder. [d] Fits with and without the closer O shell are compared to determine its effect on the hydration shell parameters. [e] Only the C and Pb shell fit values are given in the table, the notes in parentheses indicate that these parameters are used to calculate the O and OH shell parameters in the corresponding group (see text).
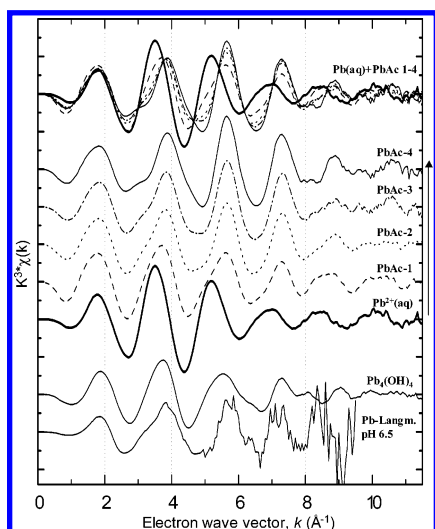

Figure 1. Data from the aqueous standards (Pb^{2+}(aq), [Pb$_4$(OH)$_4$]$^{4+}$, PbAc-*n*) and the Pb−Langmuir monolayer sample. The arrow indicates increasing Pb−acetate binding. The Pb(aq) and all PbAc-*n* data are all overlaid at the top, using the line convention from the individual spectra
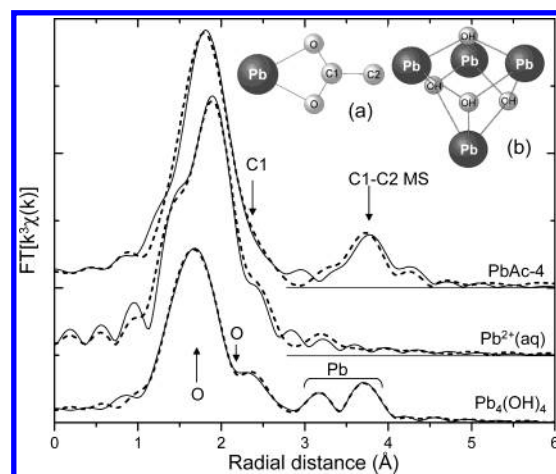

Figure 2. Aqueous Pb standards: Fourier transform ($\Delta k = 2.2-11.0$ Å^{-1}) of $k^3\chi(k)$, of experimental data (dash) and fits (solid line). These standards were considered as models for Pb bound to an acetate group (PbAc-4), hydrated Pb [Pb^{2+}(aq)], and hydrolyzed Pb, [Pb$_4$(OH)$_4$]$^{4+}$. (a) Pb bound bidentate to an acetate group. (b) Structure of the [Pb$_4$(OH)$_4$]$^{4+}$ complex.

Pb coordination, at all k weightings. The obtained coordination number and distances for Pb−Pb (Table 1) are consistent with the crystallographic data[44] and with previous XAFS studies.[43,46] The short Pb−O distance is consistent with the bridging Pb−OH bonds in the [Pb$_4$(OH)$_4$]$^{4+}$ cage, and the disordered O shell at 2.7 Å is attributed to a hydration shell around the aqueous

complex. Coordination numbers for the Pb−OH shell (O1 in Table 1) do not correlate well with the number of Pb−OH bonds in the crystal structure. This discrepancy might be caused in part by the correlation between the number and the σ^2 variables, but also by the large disorder in the shell. As discussed in previous XAFS work on model Pb compounds, the detection

of some of the atoms in a shell with large anharmonic thermal motion or large degree of distortion can be complicated or not possible at room temperature.[43,46,47] The Pb−OH bond lengths in the crystal $[Pb_4(OH)_4]^{4+}$ groups are in the range $R = 1.97-2.60$ Å, the average distance being 2.34 ± 0.15 Å. The disorder for the hydration shell is also quite large. Rather than trying to account for every possible disorder or thermal effect, we have used the obtained coordination numbers as parameters fitting well the data from the aqueous standards and quantifying the Pb−OH contribution relative to the better defined Pb−Pb coordination. We can then interpret or scale the coordination numbers of that shell in the fits of the unknown sample relative to the Pb−Pb numbers, provided that the σ^2 values are held fixed to the ones obtained in solution.

In summary, the solution standards provide spectra of Pb^{2+} atoms in several isolated environments that are likely to be present in the sample of interest. EXAFS is sensitive to the average coordination around the absorber atom, so it is important to understand the individual contributions before performing a fit of an unknown sample. Fits of the standards demonstrate the ability of the FEFF8 code to model separately a hydrated Pb ion, Pb bound to an acetate group in solution, and a hydrolysis $[Pb_4(OH)_4]^{4+}$ product. The fit values place constraints on the EXAFS structural variables, which may become correlated in samples with mixed environment or when the data range is limited.

4.2. Pb−Langmuir Monolayer Sample. *4.2.1 XANES Results.* The grazing incidence geometry allows sampling of a thin layer at the air−water interface, corresponding to the evanescent wave penetration depth. X-ray absorption near-edge structure (XANES) scans without the organic monolayer, but with the $PbCl_2$ subphase solution were performed. There was no observable absorption edge, indicating an undetectable amount of Pb in the sampled thickness. Another control measurement was performed with heneicosanol ($CH_3(CH_2)_{20}$-OH) spread over the $PbCl_2$ solution. Heneicosanol has the same hydrocarbon chain structure but lacks the carboxyl headgroup of heneicosanoic acid ($CH_3(CH_2)_{19}COOH$). Again, no absorption edge was observed. When heneicosanoic acid was spread on the solution, the data showed a clear absorption edge. This result is direct confirmation that there is considerable increase in the Pb concentration at the interface and that the charged headgroup is responsible for the metal condensation. It also shows that the XAFS data are representative of only the atoms condensed in the interfacial region and sampling of the bulk solution is not significant.

Figure 3 compares the normalized XANES data (a) and its energy derivative (b) for the standards and the Pb−Langmuir monolayer sample. Differences are observed between Pb in the +2 and +4 oxidation state. The PbO_2 standard has a pronounced preedge feature corresponding to the 2p−6s electron transition.[48] This feature is not present or is very small in Pb^{2+} compounds, where the 6s state is unavailable for a dipole transition. The XANES of the Langmuir monolayer sample does not have a preedge feature and the edge shape is very different from that of metallic Pb (not shown). It can be concluded that the oxidation state of the Pb atoms adsorbed at the interface is Pb^{2+}. This is not unexpected; however the XANES data provide unambiguous proof of this fact.

Differences can also be seen between XANES of Pb^{2+} atoms in different local environments. In the Pb(aq) standard where Pb−O interactions are electrostatic, the XANES has larger
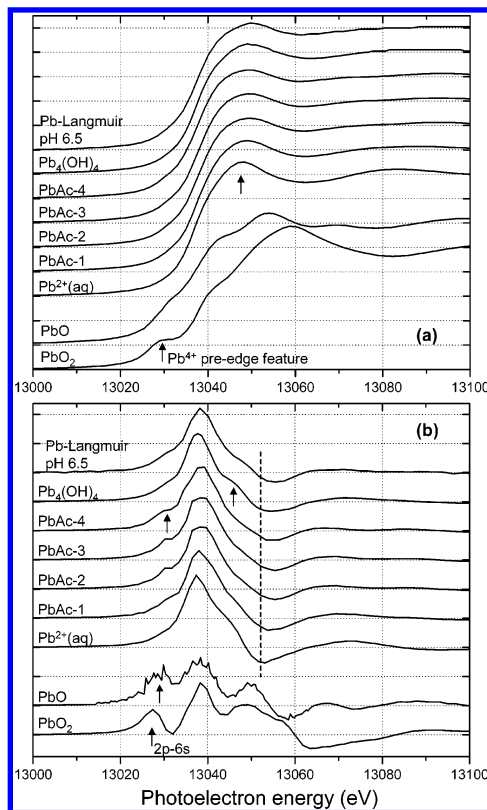

Figure 3. (a) XANES data from the Pb−Langmuir sample compared to the aqueous (Pb^{2+}(aq), PbAc-*n*, $[Pb_4(OH)_4]^{4+}$) and powder (PbO, PbO_2) standards. (b) Energy derivative of the data in (a). The arrows and the dotted line point to features that are discussed in the text.

"white line" amplitude (13048 eV). The first minimum in the XANES derivative (Figure 3b, vertical line at 13052 eV) occurs at energies slightly lower than those of the other Pb standards. Both shoulders of the main peak are featureless. In the acetate solutions, the derivative minimum shifts to higher energies (13055 eV), and a feature appears on the left shoulder of the main derivative peak (13030 eV). Differences similar to those from Pb(aq) are seen in the $[Pb_4(OH)_4]^{4+}$ sample as well; however, the feature on the left shoulder is not present and there is a concave down shape (13045 eV) on the right shoulder of the main derivative peak. A comprehensive Pb L_{III} XANES analysis of similar Pb^{2+} standards can be found in Bargar et al.[43] The authors use similarities in the XANES such as the dampened "white line" and the shift in the derivative minimum (13052 eV) as evidence of covalent binding in their samples. Furthermore, the small preedge feature in the PbO spectrum is attributed to the pyramidal tetragonal coordination of the Pb atom in this compound, which makes the 2p−6s transition possible by creating 6s vacancies through $6s-6p_z$ hybridization levels resulting from the C_{4v} symmetry. The $[Pb_4(OH)_4]^{4+}$ standard that has O in distorted trigonal pyramidal coordination around Pb does not have this feature. It is seen, however, in the PbAc-*n* standards, which is another indication of the bidentate binding of two acetate groups, resulting in 4 O atom coordination at the same distance.

The Pb−Langmuir sample data show similarities to the acetate and hydrolyzed Pb species—the derivative minimum is shifted to higher energies and the main peak in the derivative shows features seen in the lead acetate and hydrolyzed lead solutions. This indicates covalent Pb binding at the interface. The absence of the preedge feature is interpreted as a lack of pyramidal O coordination around the bound Pb^{2+} atoms.
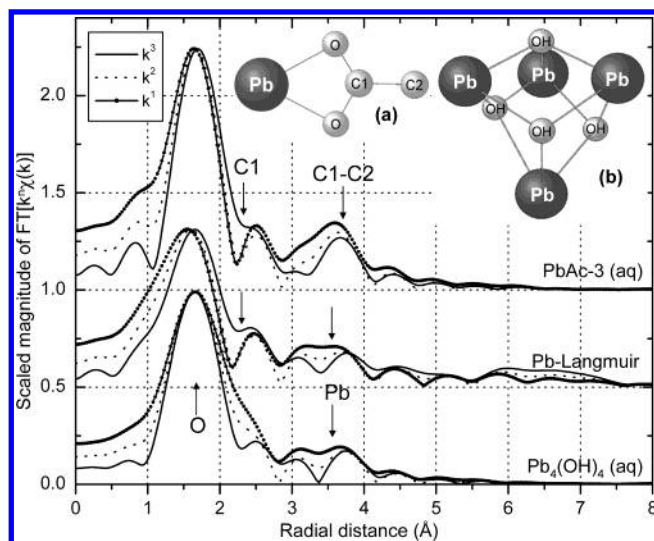
XAFS of Pb Adsorbed to Langmuir Monolayers

J. Phys. Chem. B, Vol. 107, No. 36, 2003 **9785**

Figure 4. Comparison of the Fourier transforms ($\Delta k = 2.2{-}8.0$ Å^{-1}) of $k^n\chi(k)$, $n = 1, 2, 3$, for Pb bound to an acetate group (PbAc-3), Pb adsorbed to the Langmuir monolayer (Pb–Langmuir), and hydrolyzed Pb, [Pb$_4$(OH)$_4$]$^{4+}$. The amplitudes of the transform at k^1 and k^2 weighting are scaled so the main peak is the same height as that of the k^3-weighted transform for each sample. The k^3 transforms are unadjusted and shifted vertically for clarity. (a) Pb ion bound bidentate to an acetate group. (b) Structure of the [Pb$_4$(OH)$_4$]$^{4+}$ hydrolysis complex.

4.2.2. EXAFS Analysis and Numerical Fits. The $k^3\chi(k)$ for the Langmuir monolayer sample is shown on Figure 1. Data are used only up to $k = 8$ Å^{-1} in the FT, because at higher k values the peak-to-peak variations (noise) are larger than the amplitude of the oscillation. The scaled FT magnitude at three different k weightings for the Pb–Langmuir sample and the PbAc-3 and [Pb$_4$(OH)$_4$]$^{4+}$ solutions is shown on Figure 4. The PbAc-3 is chosen for comparison among the acetate standards because its $k^3\chi(k)$ shows the greatest similarity to that of the Langmuir sample, particularly at $k = 3{-}5$ Å^{-1} (Figure 1). This is an indication of hydration water around the adsorbed Pb ions, as the PbAc-3 sample is intermediate between the PbAc-4 and Pb(aq) standards. The largest FT peak (due to O backscattering) of the monolayer sample can be seen to shift with k-weighting change, the same way it does in the acetate solution standard. The shift is caused by the interference of the O and C backscattering signals. The features at $R = 2.3$ Å that are present in both the monolayer sample and acetate standard can also be traced to the C1 atom from the carboxyl group. At larger distances (3–4 Å), the Langmuir sample resembles more closely the [Pb$_4$(OH)$_4$]$^{4+}$ standard—the peak is split and the peak height is smaller than that observed for C–C multiple scattering. The k-weight dependence is similar to the [Pb$_4$(OH)$_4$]$^{4+}$ standard. The imaginary part of the FT (Figure 5) shows similar trends. The C1 atom feature at $R = 2.3$ Å can be seen to grow with increased carboxyl binding in solution and is also present in the Pb–Langmuir sample. Between $R = 3$ and 4 Å, the Pb–Langmuir sample is similar in shape to the [Pb$_4$(OH)$_4$]$^{4+}$ standard. Additional arguments against assignment of the 3–4 Å features to linear C1–C2 multiple scattering are the sawtooth-shaped chain structure of the fatty acid[49] and the fact that the positions of the Pb ions, even though covalently bound to the headgroup at a certain distance, are also influenced by electrostatic interactions in the Stern and diffuse layer.[50] The Pb–C1–C2 angle, if at all the same for all Pb ions, is likely to be different from 180° in either case. In contrast, both the Pb atom and the acetate group are essentially unconstrained in solution
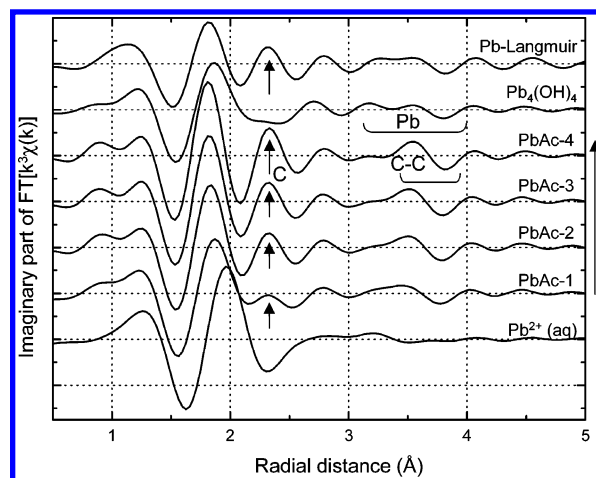

Figure 5. Comparison of the imaginary part of the FT for the Pb–Langmuir sample and the aqueous standards (Pb(aq), PbAc-n, and [Pb$_4$-(OH)$_4$]$^{4+}$). The contributions from the different shells in the standards is shown. The arrow to the right of the figure points to increasing proportion of acetate-bound Pb in the PbAc-n samples.

and a planar bidentate acetate complex with Pb–C1–C2 alignment is expected.

Two qualitative conclusions can be drawn from the observations in the FT: the immediate Pb^{2+} environment suggests carboxyl binding, and the features between 3 and 4 Å suggest the presence of Pb–Pb interactions. Theoretical modeling of the data is necessary to ascertain the qualitative findings. Standard EXAFS shell-by-shell fitting, however, is not well suited in this case. The short data range causes the contributions from the different shells to overlap in the FT, which produces correlations in the fitting parameters. This is further complicated by the mixed carboxyl-hydrolysis Pb environment suggested by the qualitative analysis. To deal with these complications, we adopt an approach in which contributions from entire entities (rather than individual coordination shells) are included in the fit. For instance, if a Pb–Pb interaction from a [Pb$_4$(OH)$_4$]$^{4+}$ entity is included, the Pb–OH interaction must also be included in the appropriate proportion, at the appropriate distance, and with the appropriate disorder; similarly, adding a Pb–C interaction from COO binding should be accompanied by appropriate constraints on the O shell. The coordination numbers of the entire entities are then varied in the unknown sample. Such an approach is in essence a linear combination fit of known spectra and rests on the assumption that the Pb–acetate and Pb–Pb interactions in solution are similar to the metal-headgroup and Pb–Pb interactions at the interface. We test this assumption by allowing the distances of the characteristic atoms in each entity to vary, as a different binding mechanism is likely to produce different bond lengths. The best fit model consists of the O and C1 shells from a carboxyl group, O1 and Pb shells from the [Pb$_4$(OH)$_4$]$^{4+}$ standard, and a hydration water O2 shell. In the carboxyl group paths, the number of O atoms is constrained to be twice the number of C atoms (bidentate binding is assumed, as suggested by the solution standards and infrared studies on a Pb–Langmuir monolayer[11]). The Pb–C and Pb–O distances are allowed to vary but the relative O–C distance is fixed. In the [Pb$_4$(OH)$_4$]$^{4+}$ paths, the number of Pb–OH interactions is constrained to be in the same proportion to Pb–Pb interactions as in the solution fit; however, the Pb–Pb coordination number is varied. A single distance change variable scaled to the distance from the absorbing Pb atom is applied for both. In the hydration O shell, the coordination number,
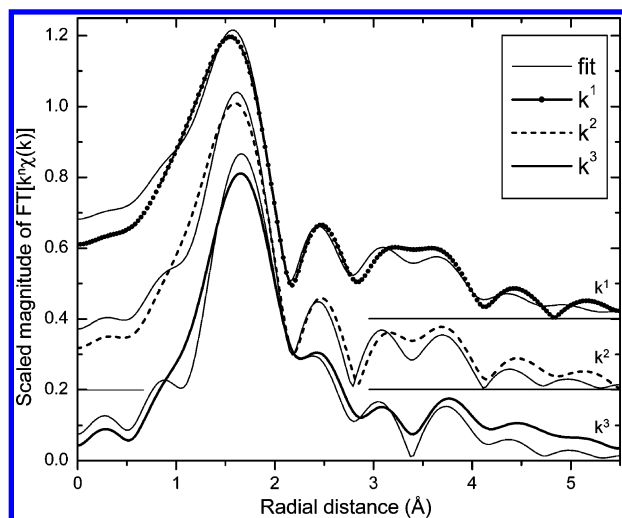
Figure 6. Fit results for the Pb−Langmuir monolayer sample. The amplitude at k^1 and k^2 weightings is scaled so that the main peak amplitudes are equal to that of the k^3-weighted transform. Spectra are shifted vertically for clarity. The fit parameters are $\Delta k = 2.2-8.0 \text{ Å}^{-1}$, $\Delta R = 1.0-4.0 \text{ Å}$.
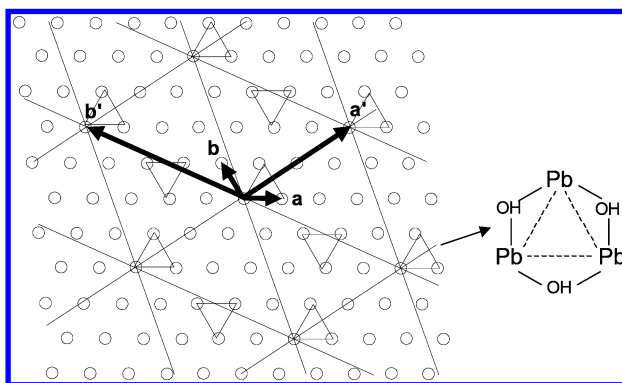

Figure 7. Schematic drawing of the proposed adsorption mechanism, viewed from under the organic monolayer. The circles represent the carboxyl headgroups and the triangles represent the proposed [Pb$_3$-(OH)$_3$]$^{3+}$ structure pictured on the right. The unit vectors are **a** and **b** for the organic lattice, and **a′** and **b′** for the superlattice. Each Pb atom binds covalently one carboxyl headgroup.

distance change, σ^2, and third cumulant parameters are all varied. In all paths of the model, the ΔE_0 and σ^2 values (except σ^2 of the hydration shell) are set to the ones obtained in the fits of the corresponding solutions. A uniform energy origin shift variable is added to all ΔE_0's.

Results from the fits are shown in Figure 6. The fit line reproduces the data features at all three of the k weightings used in the simultaneous fits. Fit parameters are listed in Table 1. The values for the distance of the C and Pb atoms are in good agreement with those found in the solution standards. The Pb coordination is 0.9 ± 0.2 carboxyl groups and 2.8 ± 0.9 Pb neighbors. These results are consistent with the adsorption of either a Pb$_3$ triangle by itself, or of the Pb$_3$ triangle that is one face of the Pb$_4$ tetrahedron in the [Pb$_4$(OH)$_4$]$^{4+}$ hydrolysis complex (Figure 4b). In the case of a Pb$_3$ adsorbent, each two Pb atoms are most likely bridged by an OH group on the side opposite the monolayer, resulting in a [Pb$_3$(OH)$_3$]$^{3+}$ complex (Figure 7). The C coordination number is consistent with one Pb ion binding one carboxyl group. The 1:1 stoichiometry is also supported by the XANES results—in the bidentate mode considered here, binding to two headgroups would result in tetragonal coordination and a preedge XANES feature. Such a feature, however, is not observed.

On Figure 7 we present a possible arrangement of a Pb$_3$ triangle relative to the monolayer lattice that is consistent with the fit results. Each Pb atom in the triangle vertexes is covalently bound to one carboxyl headgroup, resulting in 0.75 or 1.0 average coordination (for an adsorbed Pb$_4$ tetrahedron or Pb$_3$ triangle, respectively), consistent with the fitted 0.9 ± 0.2 carboxyl groups per Pb atom. The distances between the headgroups in the monolayer[17] are close to the Pb−Pb distance and allow such a configuration. Without having definitive proof for it, we propose two Pb$_3$ or Pb$_4$ clusters per unit cell of the superlattice, so better headgroup charge compensation and space filling can be achieved. The Pb clusters are likely to electrostatically repel each other, so the arrangement of Figure 7 allows for "vertex" interactions between Pb$_3$ triangles when they are close and "side" interactions when they are farther apart. Further experiments and calculations should provide more insight into the number and arrangement of these hydrolysis complexes.

The use of spherically averaged EXAFS in the analysis of the planar Pb−Langmuir sample requires justification. Because the Langmuir monolayer is a two-dimensional powder in the plane of the solution surface,[1] it has axial symmetry about the vertical direction (*z*). The incident X-ray beam is linearly polarized in the horizontal plane, so electron backscattering from atoms coordinating Pb in this plane will be enhanced relative to those that are out-of-plane. Exact treatment for an L$_{III}$ edge is complicated[51] and requires information about the angle of the Pb−carboxyl bond and of the Pb$_3$ plane, which are not known. Any polarization dependence will be observed as changes in the coordination numbers obtained in the fits. To determine the maximum possible effect, FEFF8 calculations for different orientations of the Pb−carboxyl and Pb−Pb bonds were performed. Circular averaging in the interface plane (*xy*) was done to account for the axial symmetry. Results are shown on Figure 8 for the limiting cases in the orientation. The spherically averaged spectrum can be reproduced by scaling the limiting cases up or down by no more than 20%. This limits to ~20% the maximum error in coordination numbers that could be introduced by using spherically averaged EXAFS. We estimate the uncertainty to be even lower, because the dimensions of the carboxyl lattice and Pb−Pb distance imply an intermediate angle between 0 and 90 deg for the Pb−carboxyl bond. Assuming that the Pb atoms lie in a horizontal plane and accounting for polarization will reduce the Pb−Pb coordination number in the fits closer to 2.0, making the proposed Pb$_3$ model even more consistent with the data. Taken at its largest value, the 20% uncertainty in coordination numbers is smaller than the ca. 30% error bars obtained in the fits. An exact treatment with known bond angles will therefore not change the presented conclusions, even if feasible.

4.2.3 Discussion of the Proposed Model in the Context of Previous Studies. As mentioned in the Introduction, Pb is known to affect the monolayer quite differently from otherwise similar divalent metals. Specifically, only Pb compresses the monolayer at pH as low as 4.0.[5] This is inconsistent with the ionization constants of carboxyl acids and with bulk Pb^{2+}−carboxyl stability constants[31] and can be explained by an adsorbed Pb hydrolysis complex in the following manner: when the monolayer is spread, the charged surface attracts the positive ions in the solution (Pb^{2+} and H$^+$) and produces a higher local Pb concentration close to the surface. This creates favorable conditions for the polymerization into hydrolysis complexes. The resulting +4 charges are more strongly attracted to the surface than H$^+$, effectively raising the local pH. The hydrolysis complexes are then able to bind to the deprotonated headgroups
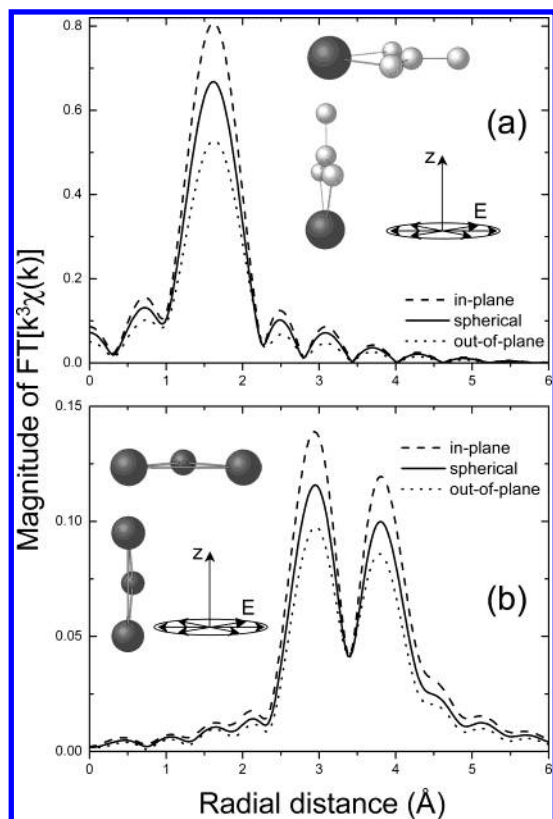
XAFS of Pb Adsorbed to Langmuir Monolayers

J. Phys. Chem. B, Vol. 107, No. 36, 2003 **9787**

Figure 8. Polarization dependence of simulated Pb−carboxyl (a) and Pb triangle (b) data. The structural parameters (N, R, σ^2) obtained in the Pb−Langmuir fit are used in the simulation and the data are Fourier transformed over the same FT range ($k^3\chi(k)$, $\Delta k = 2.2-8.0$ Å^{-1}). In-/out-of- plane indicates the electric vector being in/out of the plane of the structure, top/bottom drawing in each subfigure, correspondingly. Spherical indicates spherical averaging of the EXAFS. The circular electric polarization indicates the in-plane powder averaging of the data.

and compress the monolayer. Studies on Tb^{3+} show that the adsorption step occurs at lower pH, supporting the described mechanism for ions of larger charge.[52]

The experiments of Yazdanian et al.[5] find that the surface potential change caused by Pb saturates at much lower concentrations than Ba, Ca, Mg, Co, and Cd (Figure 5 in Yazdanian et al.[5]). This can also be explained better by a hydrolysis complex of higher charge. It is likely that the monolayer is able to attract more of the larger charge complex than the hydrated +2 cations through stronger Coulomb interaction, and the necessary amount for surface site saturation is extracted from the solution even at very low subphase concentrations.

The surface rheological properties are also affected the strongest by Pb, resulting in a film having the highest surface loss tangent ("stiffness") among Ba, Ca, Mg, Co, and Cd.[8] This supports the proposed model, as more energy is required to break the Pb−Pb or Pb−OH−Pb bonds in a Pb_3 triangle, than if single cations compress the monolayer by electrostatic attraction between the headgroups. The formation of "lines" of these complexes along the superlattice directions may also increase the stiffness of the monolayer.

The large area of the supercell ($14\times$ the headgroup unit cell area) found for Pb in the GID experiments[17] is also better explained by a large adsorption complex−such relatively long-range modulations are less likely to be caused by individual cation interactions. For comparison, Mn^{2+}, Mg^{2+}, and Cd^{2+}, which do not hydrolyze as easily, form a 1×2, 2×2, and 2×3 superlattices, respectively.[15,18]

5. Conclusions

Grazing-incidence XAFS spectroscopy can give new insight on the binding mechanism of adsorbed metals underneath Langmuir monolayers. The experimental geometry allows selective sampling of the interfacial region and enhances the signal-to-background ratio, so that spectra from a metal monolayer can be obtained. Our experiments prove directly that the charged carboxyl headgroups cause the Pb ions to segregate in the interfacial region and that their oxidation state is Pb^{2+}. Furthermore, comparisons with spectra taken from aqueous standards indicate that the adsorbed Pb is covalently bound to the carboxyl headgroups. Pb−Pb coordination at the interface is observed. Modeling of the data determines 0.9 ± 0.2 carboxyl groups and 2.8 ± 0.9 Pb neighbors in the average local environment of each Pb atom. On the basis of these results, we propose a binding mechanism for Pb as a polynuclear hydrolysis complex, rather than as individual ions. The numerical results are consistent with an adsorbed Pb triangle parallel to the interface, in a 1:1 metal:carboxyl binding stoichiometry. We discuss this possible structure in the context of previous studies on Langmuir monolayers and describe how it can explain the peculiarities observed with Pb in them. So far, infrared absorption spectroscopy studies on metal−Langmuir systems have been concentrating on the carboxyl modes, whereas Raman modes observed in $[Pb_4(OH)_4]^{4+}$ solutions standards have not been looked for. Further vibration spectroscopy studies can help elucidate the character of the Pb−Pb interactions observed by XAFS.

Supporting Information Available: Color versions of Figures 2, 4, 7, and 8. This material is available free of charge via the Internet at http://pubs.acs.org.

References and Notes

(1) Kaganer, V. M.; Mohwald, H.; Dutta, P. *Rev. Mod. Phys.* **1999**, *71*, 779.

(2) Roberts, G. G. *Adv. Phys.* **1985**, *34*, 475.

(3) Rapaport, H.; Kuzmenko, I.; Berfeld, M.; Kjaer, K.; Als-Nielsen, J.; Popovitz-Biro, R.; Weissbuch, I.; Lahav, M.; Leiserowitz, L. *J. Phys. Chem. B* **2000**, *104*, 1399.

(4) Mann, S.; Archibald, D. D.; Didymus, J. M.; Douglas, T.; Heywood, B. R.; Meldrum, F. C.; Reeves, N. J. *Science* **1993**, *261*, 1286.

(5) Yazdanian, M.; Yu, H.; Zografi, G. *Langmuir* **1990**, *6*, 1093.

(6) Kim, M. W.; Sauer, B. B.; Yu, H.; Yazdanian, M.; Zografi, G. *Langmuir* **1990**, *6*, 236.

(7) Bettarini, S.; Bonosi, F.; Gabrielli, G.; Martini, G. *Langmuir* **1991**, *7*, 1082.

(8) Yazdanian, M.; Yu, H.; Zografi, G.; Kim, M. W. *Langmuir* **1992**, *8*, 630.

(9) Zasadzinski, J. A.; Viswanathan, R.; Madsen, L.; Garnaes, J.; Schwartz, D. K. *Science* **1994**, *263*, 1726.

(10) Ghaskadvi, R. S.; Carr, S.; Dennin, M. *J. Chem. Phys.* **1999**, *111*, 3675.

(11) Gericke, A.; Huhnerfuss, H. *Thin Solid Films* **1994**, *245*, 74.

(12) Simon-Kutscher, J.; Gericke, A.; Huhnerfuss, H. *Langmuir* **1996**, *12*, 1027.

(13) Dutta, P.; Peng, J. B.; Lin, B.; Ketterson, J. B.; Prakash, M.; Georgopoulos, P.; Ehrlich, S. *Phys. Rev. Lett.* **1987**, *58*, 2228.

(14) Leveiller, F.; Jacquemain, D.; Lahav, M.; Leiserowitz, L.; Deutsch, M.; Kjaer, K.; Alsnielsen, J. *Science* **1991**, *252*, 1532.

(15) Leveiller, F.; Bohm, C.; Jacquemain, D.; Mohwald, H.; Leiserowitz, L.; Kjaer, K.; Alsnielsen, J. *Langmuir* **1994**, *10*, 819.

(16) Datta, A.; Kmetko, J.; Yu, C. J.; Richter, A. G.; Chung, K. S.; Bai, J. M.; Dutta, P. *J. Phys. Chem. B* **2000**, *104*, 5797.

(17) Kmetko, J.; Datta, A.; Evmenenko, G.; Durbin, M. K.; Richter, A. G.; Dutta, P. *Langmuir* **2001**, *17*, 4697.

(18) Kmetko, J.; Datta, A.; Evmenenko, G.; Dutta, P. *J. Phys. Chem. B* **2001**, *105*, 10818.

(19) Yamauchi, A.; Matsubara, A.; Kimizuka, H.; Abood, L. G. *Biochim. Biophys. Acta* **1968**, *150*, 181.

(20) Petrov, J. G.; Kuleff, I.; Platikanov, D. *J. Colloid Interface Sci.* **1982**, *88*, 29.

(21) Bloch, J. M.; Yun, W. B. *Phys. Rev. A* **1990**, *41*, 844.

(22) Pezron, E.; Claesson, P. M.; Berg, J. M.; Vollhardt, D. *J. Colloid Interface Sci.* **1990**, *138*, 245.

(23) Bloch, J. M.; Yun, W. B.; Yang, X.; Ramanathan, M.; Montano, P. A.; Capasso, C. *Phys. Rev. Lett.* **1988**, *61*, 2941.

(24) Watanabe, I.; Tanida, H.; Kawauchi, S. *J. Am. Chem. Soc.* **1997**, *119*, 12018.

(25) Segre, C. U.; Leyarovska, N. E.; Chapman, L. D.; Lavender, W. M.; Plag, P. W.; King, A. S.; Kropf, A. J.; Bunker, B. A.; Kemner, K. M.; Dutta, P.; Duran, R. S.; Kaduk, J. The MRCAT insertion device beamline at the Advanced Photon Source. In *Synchrotron Radiation Instrumentation: Eleventh U.S. National Conference*; Pianetta, P., Ed.; American Institute of Physics: New York, 2000; Vol. CP521, p 419.

(26) Stern, E. A.; Heald, S. M. *Rev. Sci. Instrum.* **1979**, *50*, 1579.

(27) Newville, M.; Livins, P.; Yacoby, Y.; Rehr, J. J.; Stern, E. A. *Phys. Rev. B* **1993**, *47*, 14126.

(28) Barton, S. W.; Thomas, B. N.; Flom, E. B.; Rice, S. A.; Lin, B.; Peng, J. B.; Ketterson, J. B.; Dutta, P. *J. Chem. Phys.* **1988**, *89*, 2257.

(29) http://www.ssrl.slac.stanford.edu/mes/spectra/index.html.

(30) Baes, C. F.; Mesmer, R. E. *Hydrolysis of Cations*; Wiley: New York, 1973.

(31) Martell, A. E.; Smith, R. M. *Critical Stability Constants*; Plenum Press: New York, 1974; Vols. 1−5.

(32) Stern, E. A.; Heald, S. M. Basic principles and applications of EXAFS. In *Handbook of Synchrotron Radiation*; Koch, E. E., Ed.; North-Holland: New York, 1983; p 995.

(33) Koningsberger, D. C.; Prins, R. *X-ray Absorption: Principles, Applications, Techniques of EXAFS, SEXAFS, and XANES*; Wiley: New York, 1988.

(34) Ravel, B. *J. Synchrotron Radiat.* **2001**, *8*, 314.

(35) Ankudinov, A. L.; Ravel, B.; Rehr, J. J.; Conradson, S. D. *Phys. Rev. B* **1998**, *58*, 7565.

(36) Newville, M. FEFFIT: Using FEFF to Model XAFS data. In *FEFFIT Program Documentation*, 1998.

(37) http://ixs.iit.edu/subcommittee_reports/sc/err-rep.pdf. Error Reporting Recommendations: A Report of the Standards and Criteria Committee; International XAFS Society, 2000.

(38) Bevington, P. R. *Data reduction and error analysis for the physical sciences*; McGraw-Hill: New York, 1992; p 190.

(39) Leciejewicz, J. *Acta Crystallogr.* **1961**, *14*, 1304.

(40) D'Antonio, P.; Santoro, A. *Acta Crystallogr. Sect. B−Struct. Sci.* **1980**, *36*, 2394.

(41) Rajaram, R. K.; Rao, J. K. M. Z. *Kristallogr.* **1982**, *160*, 225.

(42) Tackett, J. E. *Appl. Spectrosc.* **1989**, *43*, 483.

(43) Bargar, J. R.; Brown, G. E.; Parks, G. A. *Geochim. Cosmochim. Acta* **1997**, *61*, 2617.

(44) Grimes, S. M.; Johnston, S. R.; Abrahams, I. *J. Chem. Soc., Dalton Trans.* **1995**, 2081.

(45) Maroni, V. A.; Spiro, T. G. *J. Am. Chem. Soc.* **1967**, *89*, 45.

(46) Strawn, D. G.; Sparks, D. L. *J. Colloid Interface Sci.* **1999**, *216*, 257.

(47) Manceau, A.; Boisset, M. C.; Sarret, G.; Hazemann, R. L.; Mench, M.; Cambier, P.; Prost, R. *Environ. Sci. Technol.* **1996**, *30*, 1540.

(48) Rao, K. J.; Wong, J. *J. Chem. Phys.* **1984**, *81*, 4832.

(49) Small, D. M. *The physical chemistry of lipids: from alkanes to phospholipids*; Plenum Press: New York, 1986; Vol. 4.

(50) Adamson, A. W.; Gast, A. P. *Physical chemistry of surfaces*; Wiley: New York, 1997.

(51) Stohr, J.; Jaeger, R. *Phys. Rev. B* **1983**, *27*, 5146.

(52) Linden, D. J. M.; Peltonen, J. P. K.; Rosenholm, J. B. *Langmuir* **1994**, *10*, 1592.